**Observation of large Rashba spin–orbit coupling at room temperature in compositionally engineered perovskite single crystals and application in high performance photodetectors**

Abd. Rashid bin Mohd Yusoff[1] Arup Mahata[23] Maria Vasilopoulou[4] Habib Ullah[5] Bin Hu[6] Wilson Jose da Silva[7] Fabio Kurt Schneider[7] Peng Gao[8] Anton V.Ievlev[9] Yongtao Liu[69] Olga S.Ovchinnikova[9] Filippo De Angelis[2310] Mohammad Khaja Nazeeruddin[11]

[1]Department of Chemical Engineering, Pohang University of Science and Technology (POSTECH), Pohang, Gyeongbuk 37673, Republic of Korea

[2]CompuNet, Istituto Italiano di Tecnologia, Via Morego 30, 16163 Genova, Italy

[3]Computational Laboratory for Hybrid/Organic Photovoltaics (CLHYO), Istituto CNR di Scienze e Tecnologie Chimiche (SCITEC-CNR), Via Elce di Sotto 8, 06123 Perugia, Italy

[4]Institute of Nanoscience and Nanotechnology (INN), National Center for Scientific Research (NCSR) "Demokritos", 15341 Agia Paraskevi, Attica, Greece

[5]Environment and Sustainability Institute, University of Exeter, Penryn Campus, Penryn, Cornwall TR10 9FE, United Kingdom

[6]Department of Materials Science and Engineering University of Tennessee Knoxville, TN 37996, USA

[7]Universidade Tecnologica Federal do Parana, GPGEI, Av. Sete de Setembro, 3165, CEP 80230-901 Curitiba, Parana, Brazil

[8]Fujian Institute of Research on the Structure of Matter, Chinese Academy of Science, Fuzhu, Fujian 350002, China

[9]Center for Nanophase Materials Sciences, Oak Ridge National Laboratory, Oak Ridge, TN 37830 USA

[10]Department of Chemistry, Biology and Biotechnology, University of Perugia, Via Elce di Sotto 8, 06123 Perugia, Italy

[11]Institute of Chemical Sciences and Engineering, École Polytechnique Fédérale de Lausanne (EPFL), Rue de l'Industrie **17, CH-1951 Sion, Switzerland**

**Abstract**

Indirect absorption extended below the direct transition edge and increase in carrier lifetime derived from Rashba spin–orbit coupling may advance the optoelectronic applications of metal halide perovskites. Spin-orbit coupling in halide perovskites is due to the presence of heavy elements in their structure. However, when these materials lack an inversion symmetry, for example by the application of strain, spin–orbit coupling becomes odd in the electron's momentum giving rise to a splitting in the electronic energy bands. Here we report on the observation of a large Rashba splitting of 117 meV at room temperature, as predicted by relativistic first-principles calculations, in halide perovskite single crystals through a facile compositional engineering approach. Partial substitution of organic cations by rubidium in single crystals induces significant indirect absorption and dual peak photoluminescence as a result of a large Rashba splitting. We measured circularly polarized photoluminescence and magneto-photoluminescence in perovskite films printed by single crystals as well as magneto-electroluminescence and magneto-photocurrent in spin-LEDs based on perovskite single crystals. They indicated significant spin-momentum

locking due to the large Rashba effect. A hybrid perovskite single crystal photodetector achieved record figures of merit, including detectivity of more than $1.3 \times 10^{18}$ Jones which represents a three orders of magnitude improvement compared to the to date record. These findings show that facile compositional engineering of perovskite single crystals holds great promise for further advancing the optoelectronic properties of existing materials.

**Introduction**

Metal-halide perovskites of the general formula $AMX_3$, where $A^+$ is an organic or inorganic cation, M is a heavy metal such as $Pb^{2+}$, $Sn^{2+}$ and $X^-$ is a halide anion ($Cl^-$, $Br^-$, $I^-$), are in the forefront of current interest due to their salient features such as high absorption coefficient, long charge carrier diffusion length and low trap densities [1], [2], [3]. They are therefore considered of value in a variety of optoelectronic applications including solar cells [1], [2], [3], [4], [5], light-emitting diodes [6], [7], [8], memory devices [9], [10] and photodetectors [11], [12], [13], [14], [15], [16], [17], [18], [19], [20], [21], [22], [23], [24], [25], [26]. Spin-orbit coupling (SOC) related phenomena, such as the so-called Rashba effect, have recently gained much attention in perovskite systems as they induce intriguing optoelectronic phenomena, such as band gap narrowing and reduced non-radiative recombinations [27], [28], [29], [30]. Large Rashba splitting is mostly observed in perovskite materials that exhibit pronounced spin-momentum locking upon breaking of the inversion symmetry as in the case of two-dimensional (2D) perovskites that form multiple quantum wells where the inversion symmetry is broken naturally. Recently, a significant (*i.e.* ~40 meV) Rashba splitting close to the extrema of the electronic bands has been reported for several 2D perovskites [31], [32], [33]. This splitting induces a direct-to-indirect band gap transition which is responsible for the observed band gap narrowing and for unusually long carrier lifetime. The latter is explained on the basis of the formation of an indirect band gap below the direct transition edge that protects thermalized carriers against recombination *via* the fast direct transition [34].

Generally weak Rashba splitting has been observed in three dimensional (3D) perovskite structures [35]. These are generally quasi-cubic centrosymmetric structures, which require the application of external forces such as strain to break their inversion symmetry [36], [37], [38]. However, applying external pressure could be detrimental for practical applications. Despite the significant interest in Rashba effect related to fundamental knowledge, potential exploitation in applications requires facile methods to explore and possibly amplify this effect in perovskite materials and make use in practical devices. Intuitive strategies to achieve enhanced Rashba splitting and band gap modulation is to synthesize single crystals and/or vary the cation in A site [39]. Single crystals are prone to local inversion symmetry breaking due to structural disorder present in their surfaces [39]. Moreover, different A cation size and hydrogen bonding interactions in perovskite crystals and thin films may amplify the effect of spin–orbit coupling through affecting the crystal structure [40].

Here, we manipulate at the atomistic level the geometric environment of the perovskite structure to achieve large Rashba splitting at room temperature through a facile compositional engineering approach applied in 3D perovskite single crystals. Substitution of methylammonium (MA) and formamidinium (FA) by an optimized fraction of rubidium (Rb) cations induces a Rashba splitting which causes red shifted indirect absorption, dual peak emission at room temperature and increase in the carrier lifetime by nearly a factor of two [27], [37]. The magnitude of Rashba splitting was estimated by the energy difference of the emission peaks and found about 104 meV, which is consistent with the 117 meV calculated by first principles relativistic calculations. This is significantly higher compared to 35 meV which was predicted for

the undoped perovskite single crystals. Our experimental evidence indicates uniform Rb substitution within the crystal surface and bulk whereas circularly polarized photoluminescence and magnetic field-effect measurements verify the enhanced odd-in-electron's momentum spin–orbit coupling. Our facile methodology of enhancing the Rashba splitting through compositional engineering of the perovskite single crystals enabled direct application in practical devices. Specifically, the Rb incorporated perovskite crystals served as an optoelectronic material platform to achieve high-performance photodetection in a perovskite/molybdenum sulfide ($MoS_2$) hybrid device with detectivities exceeding $1.3 \times 10^{18}$ Jones, nearly three orders of magnitude higher than the thus far reported record of $7.5 \times 10^{15}$ Jones [11], demonstrating the potential impact of our approach in several classes of perovskite optoelectronics.

**Results and discussion**

Perovskite single crystals (SCs) of the general formula $Rb_x(MAFA)_{100-x}PbI_3$ ($x$ = 0, 5, 10, 15) were grown with an inverse temperature crystallization method in γ-butyrolactone (GBL) (Fig. S1, Supporting Information (SI)). Compositional engineering was achieved through replacing part of MA and FA cations with $Rb^+$. The small radius alkali metal $Rb^+$ was chosen to replace some of the large organic cations in order to insert a symmetry changing structural distortion into the perovskite lattice aiming at breaking the crystal inversion symmetry [41]. This could induce enhanced Rashba splitting on the otherwise spin-degenerate parabolic bands [42], [43]. The incorporation of Rb within the crystals, however, is challenging and it was accomplished by careful control of the temperature gradient whereas the crystals size was highly dependent on the Rb content. This was controlled through adjusting the precursor concentrations in the initial solution (Fig. S2). The nominal stoichiometry of perovskite SCs that gave rise to both indirect absorption at room temperature and double peak PL emission was $Rb_{15}(MAFA)_{85}PbI_3$ (termed hereafter as RbMAFA for brevity). These crystals exhibited well-defined shape and size in the micrometer scale (Fig. 1a). They were of fine quality as evidenced by the selective area electron diffraction (SAED), the low-energy electron diffraction (LEED) patterns, the high-resolution TEM (HRTEM) image and the X-ray diffraction (XRD) patterns (Fig. S3a-d and Fig. 1b). The crystal lattice of these crystals was affected by Rb incorporation as evidenced by the shift towards higher angles of the XRD peaks (Fig. 1b). For the undoped crystals (termed hereafter as MAFA), the peak at 13.83° is attributed to (0 0 1) plane. This peak shifts to 13.94° for RbMAFA single crystals, which indicates a small decrease in the lattice volume upon the incorporation of the smaller $Rb^+$ ion. Even a small lattice distortion, however, could be sufficient to induce enhanced Rashba splitting through breaking of inversion symmetry of the crystal [40], [41], [44]. Since X-ray diffraction represents a bulk analysis method, we speculate that Rb incorporation also proceeds within the bulk and it is not only limited in the surface of the crystals. To unravel, however, if this incorporation is uniform, we performed elemental analysis in the MAFA and RbMAFA SCs using time-of-flight secondary ion mass spectrometry (TOF-SIMS) measurements. The TOF-SIMS profiles verified that there are no Rb cations in the undoped samples, while Rb cations are incorporated into the perovskite lattice quite uniformly and do not form aggregates in the interspace. This was partially corroborated by TOF-SIMS images that show the surface (Fig. 1e,f) and the inner within 50 μm zoom-in (Fig. 1 g,h) of the RbMAFA samples. Similar measurements were obtained in the undoped samples (Fig. S4). It is observed that Rb incorporates on the surface and inside the lattice of the doped crystals. This was also supported by electron dispersion spectroscopy (EDS) mapping (Fig. 1 i–l). As a result, we expect that with our method we are able to induce compositional tuning within the bulk and surface of these crystals.

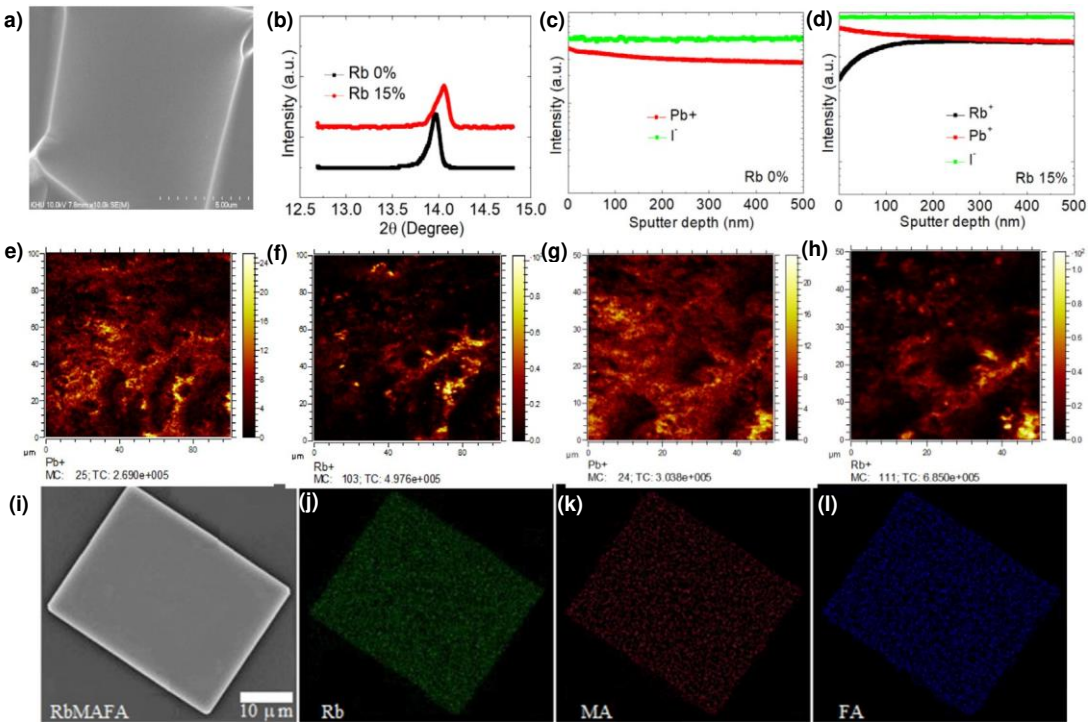


Figure 1. Structure and elemental analysis of perovskite single crystals. (a) SEM image of a typical $Rb_{0.15}(MAFA)_{0.85}PbI_3$ (15% Rb) single crystal. (b) Powder XRD patterns of MAFA (0% Rb-undoped) and RbMAFA (15% Rb-doped) perovskite single crystals. Elemental analysis of perovskite single crystals: TOF-SIMS depth profile results for (c) MAFA (0% Rb) and (d) RbMAFA (15% Rb) single crystals. TOF-SIMS imaging data for RbMAFA (10% Rb) single crystals collected on the surface (e, f) and with 50 µm zoom-in (g, h). (e, g) Show the $Pb^+$ distribution and (f, h) the $Rb^+$ distribution. (i) SEM image and (g–l) the corresponding EDS mapping of a representative RbMAFA (15% Rb) perovskite crystal.

Next, we were able to deposit printable perovskite films of high quality from these crystals using a doctor blade technique (Fig. S5). Fig. 2a presents the UV–Vis absorption spectrum of a perovskite film deposited from RbMAFA SCs. Remarkably, the absorption spectrum extends far into the near-infrared region with the absorption onset reaching ~900 nm. This extension in the absorption onset is surprising, as incorporation of smaller Rb cations should induce band-gap opening due to structural distortion [45], [46]. The observed absorption shift can be attributed to either gap states lying below the bands extrema or to indirect tail states lying below the indirect transitions [47], [48], [49]. However, trap states cause undesirable recombinations hence decreasing carrier lifetime. Transient photoluminescence (TRPL) decay curves measured at room temperature in films composed of RbMAFA and MAFA SCs (Fig. 2b) indicate a strong increase in carrier lifetime in the 15% Rb-doped SC films. The TRPL were fitted with two exponentials each and the fitting parameters and estimated carrier lifetimes are summarized in Table S1. A nearly 100% enhancement in carrier lifetime of RbMAFA compared to MAFA perovskite (from 46.34 to 81.33 ns) denotes that the below band gap transitions in the compositionally engineered perovskite are not likely to originate from trap states as they would decrease the charge carrier lifetime. Further evidence for the existence of strong indirect transitions in the Rb-engineered perovskite SCs were obtained by the room temperature steady-state PL spectrum taken in films composed of RbMAFA SCs (Fig. 2c). Remarkably, the PL spectrum presents dual emission consisting of a main peak centered at 762 nm (1.627 eV) and a second, weaker but distinct peak at 814 nm (1.523 eV). Recently, Wang et al. [27], and Grätzel and co-workers [37], attributed the dual peak PL to the direct and indirect band gap emission in $MAPbI_3$ films and $APbBr_3$, where A corresponds to caesium, MA or FA, single crystals, respectively. The indirect band gap was originated

from enhanced Rashba splitting upon breaking the crystal centrosymmetry. Similar direct and indirect dual emission peaks have also been reported in conventional indirect semiconductors such as germanium (Ge), gallium selenide (GaSe), and 2D transition metal dichalcogenides ($MoS_2$, $MoSe_2$) [50], [51]. We therefore believe that our results indicate a significant Rashba splitting in the Rb-engineered perovskite SCs which causes the formation of tail states with an exponential distribution below the direct band gap. The effect should be stronger at the conduction band minimum (CBM) because the atomic number of Pb (Z = 82), the orbitals of which have major contribution in the conduction band minimum, is larger than I (Z = 53). We calculated the energy Rashba splitting from the energy difference between the two peaks in the dual peak PL spectrum of RbMAFA SC film and found it to be ~104 meV.

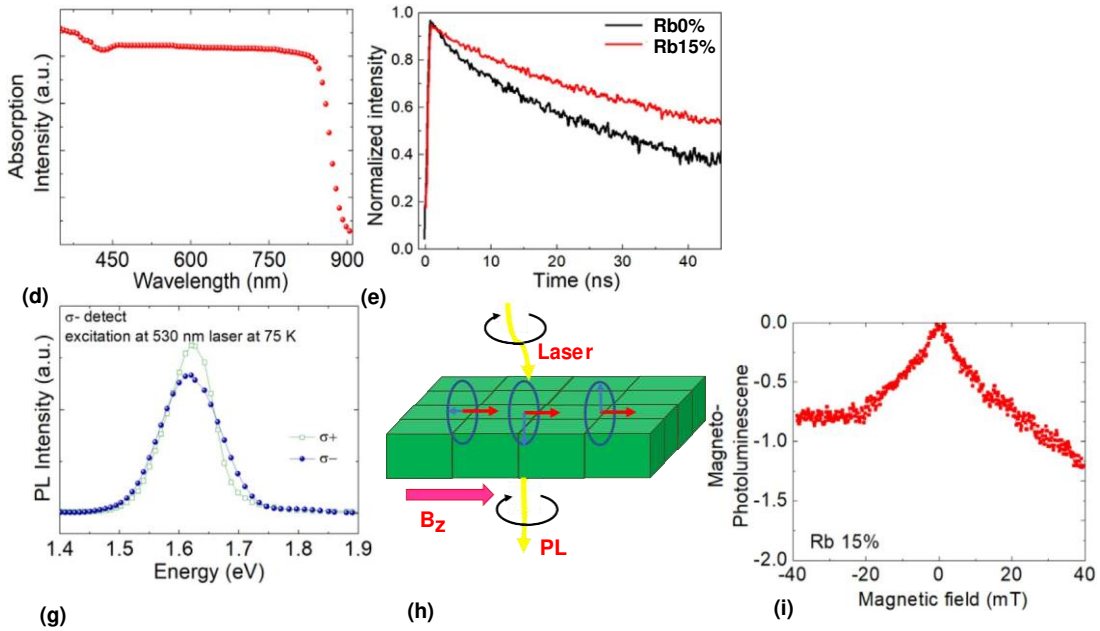


Figure 2. Optical and magnetic field dependent measurements. (a) UV–Vis absorption spectrum of films printed from 15% RbMAFA perovskite single crystals. (b) TRPL decay profiles of films printed from MAFA (0% Rb) and RbMAFA (15% Rb) perovskite single crystals. (c) Steady-state PL spectra of films printed from 0% and 15% Rb-doped perovskite single crystals. Two distinct absorption peaks one intense located at higher energy (i.e., 1.627 eV) and one weak located at higher energy (i.e., 1.523 eV) are evident. (d) Circularly polarized photoluminescence spectra of a RbMAFA perovskite film taken upon polarized excitation ($\sigma^-$) at 75 K. (e) Schematic set-up of measuring magneto-photoluminescence in RbMAFA perovskite films. (f) Magneto-photoluminescence response of a perovskite film printed from 15% Rb-doped perovskite single crystals. (g) Schematic illustration of the spin-LED device. (h) Magneto-electroluminescence and (h) magneto-photocurrent of the spin-LED based on 15% Rb-doped perovskite single crystal emitter (absorber) layer.

To confirm the existence of spin-dependent band splitting due to significant Rashba effect in our doped perovskite crystals, we applied circularly polarized photoluminescence spectroscopy at low temperature (75 K). The films were excited with a circularly polarized ($\sigma^-$excitation) laser at 530 nm. The circularly polarized photoluminescence components PL($\sigma^-$) and PL($\sigma^+$) present distinct difference (Fig. 2d), which originates from optical orientation and detection of spin-polarized electrons as a result of enhanced spin–orbit splitting. Next, the single crystal perovskite films were placed inside a magnetic field, $B_z$, oriented perpendicularly to the PL light propagation direction (Fig. 2e). When this perpendicular to electron spin magnetic field increases, the measured magneto-photoluminescence decreases because the external

field causes the precession of the electron spin (Fig. 2f). We further examined the magnetic field spin precession by studying spin-dependent optoelectronic characteristics in a single crystal perovskite spin-LED. The device included a perovskite film inserted between a thin ferromagnetic (NiFe) and a silver electrode. We expected that the applied magnetic field will modulate the optoelectronic properties of the device. As Rashba splitting is present in our crystals, the large spin–orbit coupling will become odd in the electron momentum. Through the magnetic field we induce changes in the spin-momentum pair with different spin configurations thus changing the electroluminescence emission (taken by applying a forward bias) or the device photocurrent (taken by illumination and application of a reverse bias) [52], [53]. The magnetic field is aligned perpendicular to the electrodes which means that it is aligned with the propagation direction of the injected carriers [54]. Spin polarized holes are injected from the ferromagnetic electrode whereas unpolarized electrons are injected from the silver electrode (Fig. 2g). Only electron-hole pairs of the same spin can form excitons which means that the electroluminescence increases as the magnetic field increases because the hole population also increases (Fig. 2h). As a result, magneto-electroluminescence appears with opposite polarity compared with that of magneto-photoluminescence as well as magneto-photocurrent (Fig. 2i). We also note that, electroluminescence originates from electron-hole pairs formed upon carrier injection that should be both triplet and singlet in nature with a ratio 3:1. In contrast, magneto-photoluminescence in the perovskite film and magneto-photocurrent in the complete device come from electron-hole pairs generated after photon absorption and present solely in the singlet configuration. This explains their similar polarity that is opposite to that of magneto-electroluminescence.

Our experimental results indicated that due to a non-centrosymmetric crystal environment upon Rb doping, spin-polarized bands whose minima are shifted in momentum space are present in RbMAFA crystals (Fig. 3a). The figure of merit of the Rashba effect is in this case defined as the Rashba interaction parameter, α. To investigate the effect of structural distortion introduced in the perovskite host by Rb incorporation, we carried out relativistic Density functional theory (DFT) calculations on (MAFA)$PbI_3$ and on $Rb_x(MAFA)_{1-x}PbI_3$ perovskites based on 2 × 2 × 1 supercell containing 16 formula units [55], [56], [57], [58], [59]. We start by investigating the 50:50 MAFA perovskite experimentally characterized considering various mutual positions of MA and FA molecules. We found three representative structures which are very close in energy (within 10 meV per formula unit) characterized by a small Rashba parameter (Fig. 3b–d, Fig. S6 and Table S2), suggesting a small inversion symmetry breaking due to the size mismatch between MA and FA cations. Starting from these three parent structures, we investigate the effect of 12.5% Rb incorporation, close to the nominal 15% Rb doping experimentally introduced. We have performed an extended structural sampling of all the possible geometries corresponding to the specific Rb doping, finding overall nine possible structures whose energy is within 34 meV, Fig. 3 and Figs. S7–S9 and Table S3. It is interesting to notice that for each of the Rb-containing structures a higher $\alpha$ value than the corresponding parent structures is predicted, clearly indicating that incorporation of Rb ions strongly enhances the Rashba effect in the considered perovskite host. As an example, for the most stable RbFAMA structure the Rashba interaction parameter increases from 1.00 to 1.24 eV Å compared to the parent MAFA structure, while maximum values of 1.00 and 1.62 eV Å are found considering slightly less stable FAMA and RbFAMA structures, respectively, see Fig. 3 and Table S3. We have stepped forward to investigate the Rashba effect with higher Rb concentration by doping three Rb atoms in the same supercell, thus modeling the composition $Rb_{0.19}MA_{0.44}FA_{0.37}PbI_3$ and $Rb_{0.19}MA_{0.37}FA_{0.44}PbI_3$. Optimized geometries, energetics and Rashba parameters for these configurations have been reported in Figs. S10–S15 and Tables S4 and S5. Notably, further Rb addition does not generally lead to increased Rashba interaction parameter, suggesting that an optimal doping density related to a maximum structural asymmetry is to be predicted.

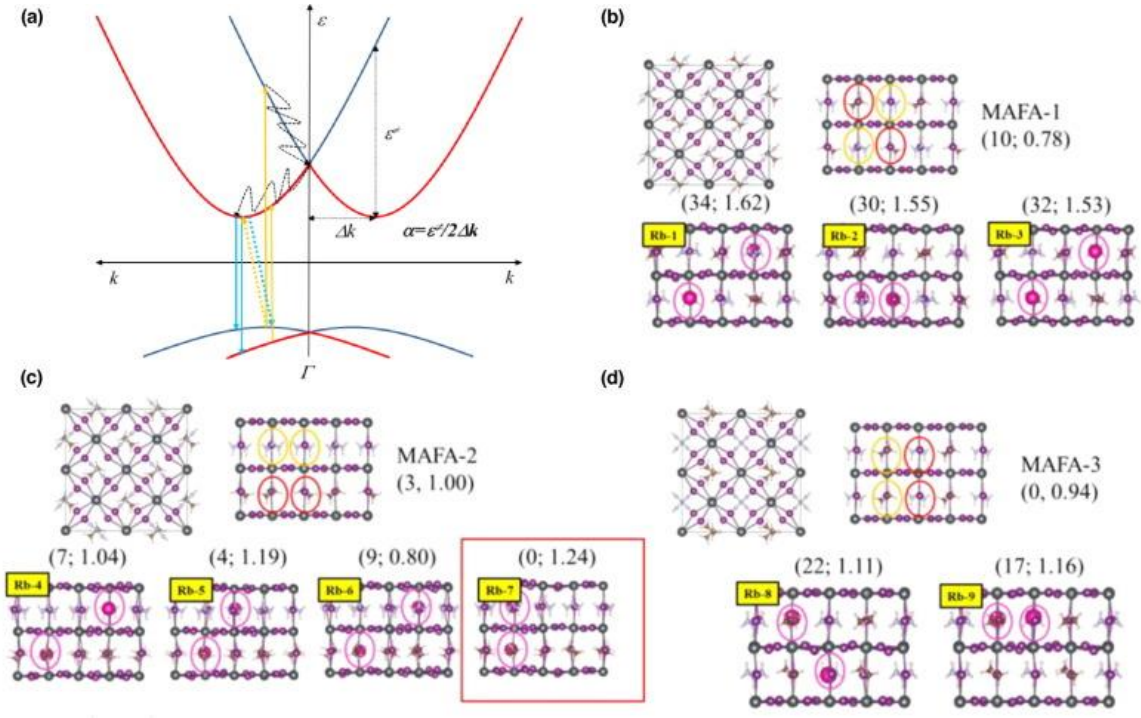


Figure 3. Rashba spin–orbit splitting. (a) Diagram of SOC-splitted Rashba bands. Both valence and conduction band are split away from the Γ point, leading to VBM and CBM which are shifted in k-space by $\Delta k$. The characteristic band energy splitting at the CBM ($\varepsilon^{*}$) is also shown for the conduction band. The blue and red bands correspond to the different spin channels. The orange and cyan arrows indicate absorption and emission pathways, both direct, *i.e.* preserving $k$ (solid) and indirect (dashed). Relaxation pathways of excited electrons are shown as dashed wavy lines. The Rashba interaction parameter is defined accordingly as $\alpha = \varepsilon^{*}/2\Delta k$. (b–d) Modulation of the Rashba effect by structural sampling. Different configuration of $Rb_{0.12}MA_{0.44}FA_{0.44}PbI_3$ modeled by doping with 2Rb atoms in 2 × 2 × 1 supercells containing 16 formula units. For each parent MAFA structure various mutual positions of Rb cations have been explored. The values in parentheses are calculated energy difference from the most stable calculated structure in meV (0 thus corresponds to the minimum energy structure). Highlighted are the position of representative MA and FA cations (orange and red, respectively) and of doping Rb cations (magenta).

The increased Rashba effect found by optimized Rb incorporation could explain the prolonged carrier lifetime and below band gap absorption upon Rb incorporation observed experimentally. The formation of an indirect band gap below the direct one may induce below band gap absorption and contribute to suppress carrier recombination by making the band-edge transitions spin- or momentum-forbidden; excited electrons may thus prefer to relax into the direct band edge and then radiatively recombine. The latter can explain the large expansion in carrier lifetime of RbMAFA. The dual emission can be explain in the context of the direct (intense) and indirect (weak) emission. The incorporation of $Rb^{+}$ defines the spin textures of the electronic bands by inducing Pb and I displacements that breaks the inversion symmetry as confirmed with DFT calculations. Based on these results, we attempted to make practical use of the significant Rashba splitting obtained in the Rb incorporated perovskite by designing and fabricating a hybrid photodetector using absorber layers composed of MAFA and RbMAFA crystals based absorber combined with a $MoS_2$ conductor. The 2D $MoS_2$ monolayer was successfully grown on the $SiO_2$/Si substrate (Fig. S16), through exfoliation, to act the device photocurrent channel towards the electrodes due to its higher carrier mobilities compared to perovskites [60]. The device geometry is presented in Fig. 4a and was designed based on the consideration that the perovskite SCs absorbs the incident light and

produces free carriers. Then, these carriers diffuse without being recombined and transfer to the $MoS_2$ monolayer due to favorable energy level alignment at the perovskite/$MoS_2$ heterointeface (Fig. 4b). Subsequently, the electrons and holes are swept by the electric field in the Ti/$MoS_2$ and Au/$MoS_2$ junctions and collected at the respective electrodes (Fig. 4c). Current-voltage (I-V) characteristic curves of the RbMAFA perovskite photodetector measured under dark and upon various light intensities are shown in Fig. 4d. In Fig. S17b similar I-V curves under weak-light conditions are also presented. These characteristics show linear and low resistance symmetric behavior upon illumination verifying that our hybrid device works as an ultra-sensitive broadband photodetector. The dark current was found lower than $10^{-12}$ A consistent with the superior crystalline quality of our perovskite. The dramatic increase in photocurrent for mild illumination conditions highlights the essential role of Rashba splitting for increased carrier generation (i.e. indirect below band gap absorption) and prolonged carrier transport in achieving high photoconductivity.

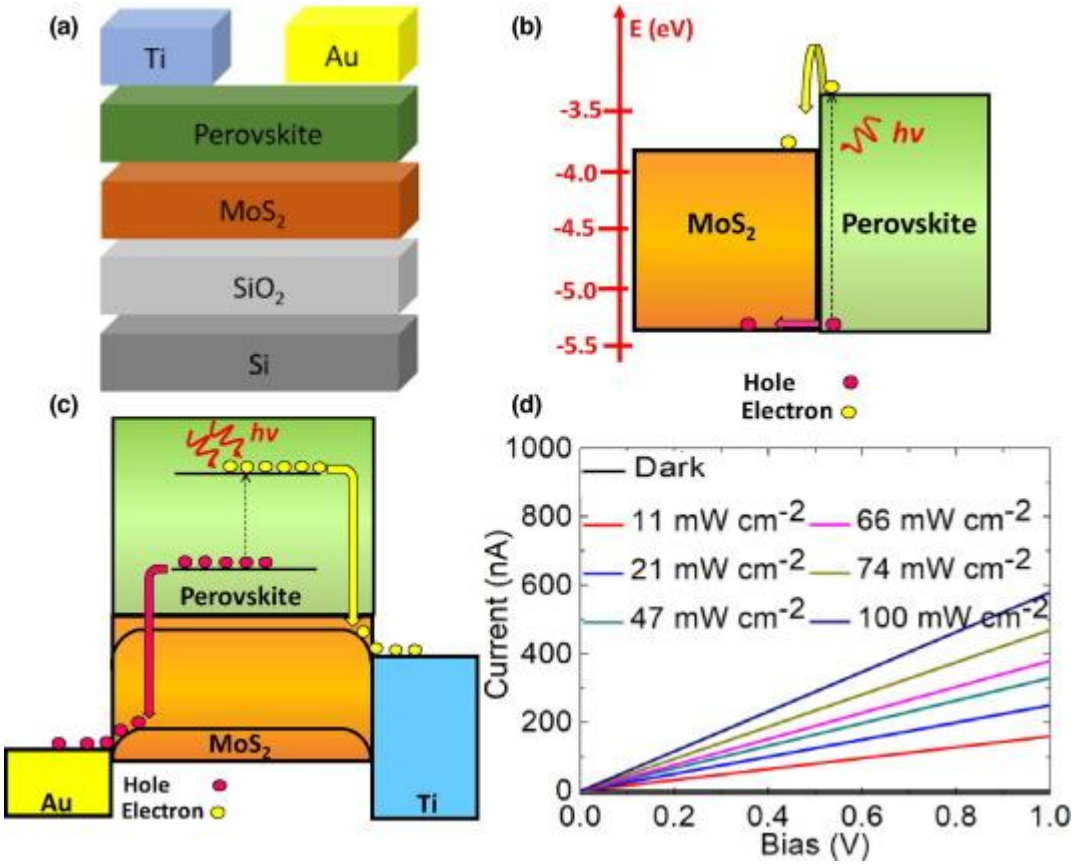


Figure 4. Photodetector configuration and working principle. (a) The device architecture of the hybrid perovskite/$MoS_2$ photoconductor type photodetector. (b) Schematic of energy-band diagram of the perovskite/$MoS_2$ interface considering vacuum level alignment before contact, and (c) illustration of the operation mechanism of the perovskite/$MoS_2$ hybrid photodetector under illumination. (d) I-V curves of the hybrid perovskite photodetector measured under various intensities of light.

In Fig. 5a the photocurrent and responsivity, which is the direct measure of the device response to light, of the RbMAFA SC perovskite photodetector under various light intensities are presented. The device responsivity R, calculated by $R = J_{ph}/L_{light}$, where $J_{ph}$ is the photocurrent and $L_{light}$ is the incident light intensity (see Methods), was found $2.4 \times 10^4$ A $W^{-1}$ that is above the to date record of $1.5 \times 10^4$ W $A^{-1}$ [11]. The decrease in responsivity in high light intensities is in agreement with an enhancement of many-body interactions in the lead halide perovskite that shorten the excitons and free carriers lifetime under high

irradiances. Furthermore, we measured the key figure-of-merit parameter of a photodetector that is its specific detectivity ($D^*$). With the synergy of a highly boosted photocurrent due to Rashba effect and low dark current derived from the superior crystalline quality of our perovskite, we evaluated a $D^* \sim 1.3 \times 10^{18}$ Jones (cm $Hz^{1/2}$ $W^{-1}$). This value is nearly three orders of magnitude higher than the to date perovskites record of $7.5 \times 10^{15}$ Jones [11], and almost five orders of magnitude higher than that of the commercially available silicon photodiodes ($\sim 3 \times 10^{12}$ Jones). This remarkable performance could be the result of the intense below band gap absorption and highly prolong carrier lifetime caused by the giant Rashba splitting of our perovskite SCs. Notably, the photodetector using MAFA SC perovskite absorber exhibited inferior performance with a maximum responsivity of 0.281 W $A^{-1}$ and maximum detectivity of $2.6 \times 10^{10}$ Jones (Fig. S17a), further corroborating the importance of using enhanced Rashba splitting in practical applications. The RbMAFA device voltage measured across the perovskite under various intensities of light in voltage detection mode and changes in the measured voltage (ΔV) and voltage responsivity of the device at different light intensities are shown in Fig. 5b,c. We estimated a high voltage responsivity of 1.9 V $mW^{-1}$ $cm^{-2}$. The response speed of the device was measured by recording the current temporal photo response (Fig. 5d, blue curve. The illumination power of a frequency modulated light of 532 nm laser was 0.3 mW. The green curve corresponds to the laser on–off). The rise/erase time of the present device was determined from the current transit time and found ~130 ms (Fig. S17c). This is highly improved compared to previously reported polycrystalline $MAPbI_3/MoS_2$ hybrid photodetectors suggesting that it is possible to further increase the device response speed by using crystals with superior quality.

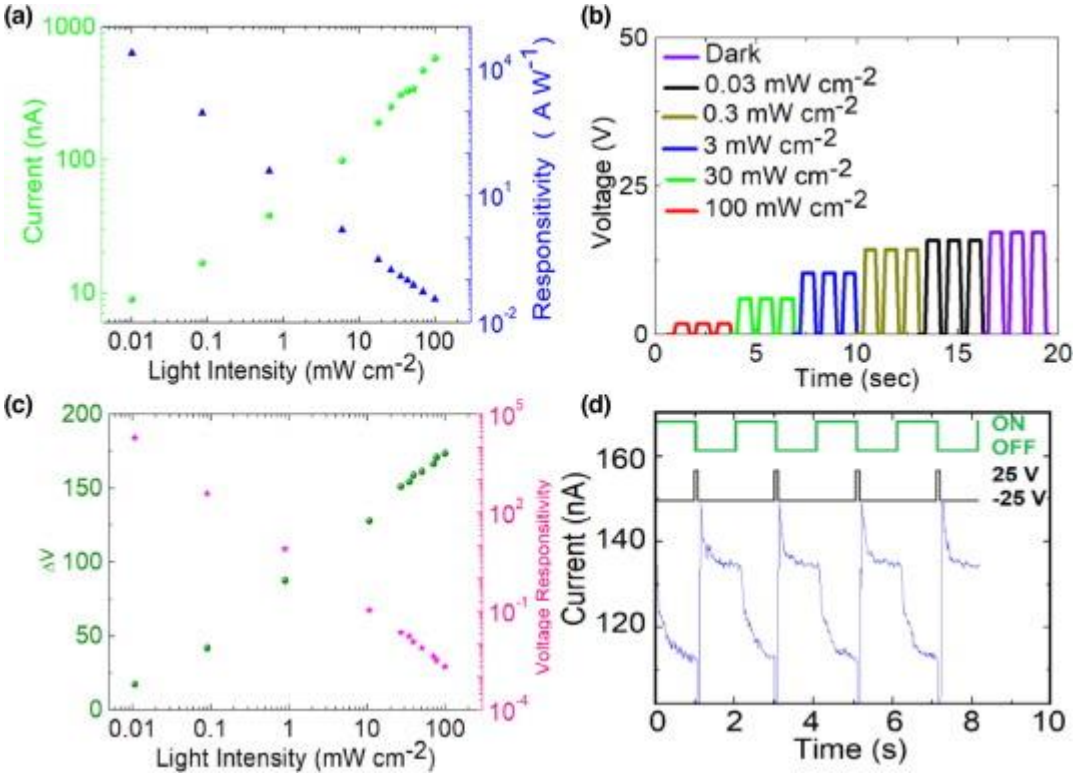


Figure 5. Performance of hybrid perovskite single crystal photodetector.
(a) Photocurrent and responsivity of the photodetector under various intensities of light. (b) Photodetector device voltage measured across the perovskite under various intensities of light in voltage detection mode. (c) Change in the measured voltage (ΔV) and voltage responsivity of the device at different light intensities. (d) Temporal photoresponse of the perovskite photodetector (blue curve). The illumination power is 0.3 mW and the laser wavelength is 532 nm. The laser on–off (green curve) is controlled by a mechanical shutter synchronized with the reset back gate voltage pulses (black curve).

## Conclusions

In summary, compositional engineering of perovskite single crystals provides a facile route for the generation of a large Rashba splitting in these crystals. Tailored Rb incorporation within the lattice of $MAFAPbI_3$ single crystals breaks the inversion symmetry hence inducing an experimentally estimated Rashba splitting of 104 meV. Theory predicts Rashba splitting up to 117 meV with a Rashba parameter of 1.62 eV·Å. TOF-SIMS and EDS measurements suggest that Rb is uniformly incorporated within the whole crystal lattice which means that the large Rashba splitting is not limited only on the crystals' surface. Circularly polarized photoluminescence and magnetic field-effect measurements verify the spin dependence in emission and photocurrent of perovskite films and spintronic devices. The compositionally engineered crystals serve as an optoelectronic material platform for the fabrication of perovskite/$MoS_2$ hybrid photodetector with above state-of-the art figure of merits including the highest detectivity ever reported for any type of perovskite photodetector. The perovskite compositional engineering paradigm presented here that induces the formation of large Rashba splitting provides a facile approach to realize not only record performance photodetection but also novel perovskite devices including optoelectronics and spintronics.

## Experimental section

**Materials.** The organic cation salts formamidinium iodide (FAI) and methylammonium iodide (MAI) were purchased from Dyesol. The lead iodide compound was from TCI, and RbI was from abcr GmbH. All chemicals were used without further purification.

Growth of single crystal perovskite. $Rb_x$**(**$MAFA)_{1-x}PbI_3$ perovskite single crystals were grown using an inverse temperature crystallization (ITC) method with some modifications. The $MAPbI_3$ (containing 1 M MAI and $PbI_2$ in GBL) and $FAPbI_3$ (containing 1 M FAI and $PbI_2$ in GBL) solutions were mixed in a 1:1 ratio. To this mixture, 1 and 1.5 M RbI solutions (containing RbI in GBL) were added to obtain perovskites with different stoichiometries (5% RbI:$(MAFA)PbI_3$ = 5:95 (v/v), i.e., $Rb_5(MAFA)_{95}PbI_3$; 10% RbI:$(MAFA)PbI_3$ = 10:90 (v/v), i.e., $Rb_{10}(MAFA)_{90}PbI_3$; 15% RbI:$(MAFA)PbI_3$ = 15:85 (v/v), i.e., $Rb_{15}(MAFA)_{85}PbI_3$). The perovskite with nominal stoichiometry $Rb_{15}(MAFA)_{85}PbI_3$ (termed as RbMAFA in this paper) gave the best photodetector performance and higher Rashba splitting. All solutions were heated at 70 °C for 24 h (in ambient condition with 35–40% relative humidity) and filtered using a hydrophobic polytetrafluoethylene (PTFE-D) filter with 0.2 µm pore size. The filtrate of mixed $Rb(MAFA)PbI_3$ solution (3 mL) was stored in a convection oven at 130 °C for 6 h.

**Preparation of single crystal perovskite films.** The precursor single crystal solution was dropped onto the $SiO_2$/Si substrates and swiped linearly at a speed of 1.2 cm $s^{-1}$ at the gap between substrates, and the blade was 80 mm. The substrates were held at *in situ* annealing during blade deposition (typically 125 °C). A 10–20 µL of precursor solution was used per 2.25 $mm^2$ substrate. This value was much lower than 50–100 µL typically used for spin coating of similar perovskite solutions over the same area of substrate, which demonstrated the advantages of high material usage by doctor-blade coating. After rolling was complete, the substrates were cooled immediately to avoid the possibility of thermal decomposition. All experiments were conducted under ambient conditions.

**Structural and optical measurements.** Perovskite thin films were characterized using an optical microscope (ICS-305B, Sometech) and a scanning electron microscope (SEM, Hitachi S4800) with an accelerating voltage of 15 kV. The optical properties were measured using a UV–visible spectrophotometer (Varian Cary 5000, Agilent Technologies) and a fluorescence spectrometer (FLSP920, Edinburgh Instruments). Steady-state PL measurements were acquired using a time correlated single photon counting setup. The samples were photoexcited using a laser head pulsed, providing <200 ps pulses with the fluence of ~30 nJ/cm$^2$. The PL excitation wavelength was 530 nm. The time resolved photoluminescence (TRPL) was measured using a commercial time-correlated single-photon counting system (FluoTim 200, PicoQuant). The crystallinity and elemental analysis of the thin films were determined via SAED and EDX spectrometry (AZtec software, Oxford instruments) with a transmission electron microscope (TEM, JEM 2100F, JEOL.) at an accelerating voltage of 200 kV. For preparing the TEM sample, the focused ion beam process was applied (Nova 600, Nanolab). Large-area crystallinity was measured by an X-ray diffractometer (D/MAX-2500/PC, Rigaku) using a Cu Kα source ($\lambda$ = 1.54 Å) operated at 2.4 kW and an HR X-ray diffractometer (Smartlab, Rigaku) with a 2D detector (PILATUS 100 K, Rigaku) using a Cu Kα source operating at 9 kW. For the in-plane phi scan, the 2$\vartheta$ angle was fixed at 14°. For the 2D XRD measurements, the X-ray analyzed area of the film was 5 mm × 5 mm. The measurement range was from 10° to 55° in the 2θ direction and from 0° to 60° in the chi direction.

**Elemental analysis.** The time-of-flight secondary ion mass spectroscopy (TOF-SIMS) depth profiles were collected using a TOF analyzer (TOF-SIMS 5, Ion-TOF GmbH), equipped with a 25 keV $Bi^+$ beam for the analysis and a 1 keV $Cs^+$ and $O_2$ source for the sputtering. TOF-SIMS images were taken TOF.SIMS.5.NSC instrument (ION.TOF Gmb) (Primary gun $Bi_3^+$, spectral mode: 30 keV, 30 nA, 5 µm spot size, imaging mode: 30 keV, 0.5 nA, ~120 nm spot size). Energy dispersive spectroscopy (EDS) was conducted by using an EDS device connected to SEM.

**Photodetector fabrication.** Bottom-contact, top-gated FET photodetectors were constructed on Au (50 nm) electrodes (the separated spacing and width of this finger electrode were 5 µm, and the effective area was 3 × 10$^5$ µm$^2$) that were patterned by photolithography on a $SiO_2$ (500 nm)/Si (p-doped) substrate. The clean pre-patterned (in acetone, toluene and isopropyl alcohol for 15 min each, dried in an oven at 120 °C for 15 min) and exposed for 1.5 h to UV light in air $SiO_2$ substrate surfaces were treated with decyltrichlorosilane (DTS) for 0.5 h by immersion in 1% by volume of DTS in toluene. POCB (3 µL) was spin-coated on the $SiO_2$/Si-treated OTS. Monolayer $MoS_2$ were mechanically exfoliated from commercially available molybdenite crystals (Furuuchi Kagaku, Japan) and were later analyzed using optical microscopy, Raman, and PL spectroscopy. The single crystal perovskite film was deposited on the top of the finger electrode. The samples were annealed at 80 °C for 30 min and kept under high vacuum (10$^{-7}$ Torr) overnight (>10 h) to remove any residual solvent. The 40 nm Au electrodes were deposited on top of perovskite layer by thermal evaporation.

**Electrical characterization of the photodetectors.** The photodetectors were characterized using a probe station at ambient condition. A red LED (OVLBx4C7 Series, OPTEK Technology Inc., main wavelength: 623 nm) was mounted above the photodetector, which was controlled by a Keysight precision source/measure unit (B2902A) in the current source mode. The optical power density that reached the sample surface was determined by measuring a commercial reference photodiode (PDB-C154SM, Luna Optoelectronics) with a responsivity of ≈0.3 A W$^{-1}$ at 623 nm. The single crystal photodetector response was measured with a semiconductor device analyzer B1500A (Agilent Technologies), and the overall measurement scheme was controlled via MATLAB. The extraction of the

time constant was performed by modulating the LED voltage with an Agilent waveform generator (33522A) and constantly applying 100 mV to the photodetector with the Keysight precision source/measure unit (B2902A). The voltage was applied on the photodetector top electrode. At the bottom electrode, a current amplifier (Stanford Research Systems, Model SR570) was connected, which converted the current to a voltage for the display on the oscilloscope (Agilent Technologies, MSO-X 3014A).

**Magnetic measurements.** The magneto-photoluminescence (MPL) measurements were performed in a single crystal perovskite film using solid-state laser operating at 488 nm as a pump excitation. The MPL is defined as:

and was measured at a constant laser excitation.

The device for magnetic measurements was fabricated as follows: a thin (about 10–15 nm) ferromagnetic NiFe (Angstrom Engineering, 99.99% purity) film was deposited on single crystal RbMAFA (15% Rb) perovskite layer using electron beam evaporation with a base chamber pressure of $1 \times 10^{-7}$ Torr and deposition rate of 0.1 Å $s^{-1}$. Silver paste was later applied on both sides of the device to provide electrical contact. The single crystal perovskite device was transferred into a vacuum chamber that was place in a magnetic field provided by an electromagnet up to 40 mT. The magneto-photocurrent was measured upon illumination at room temperature. The magneto-electroluminescence (MEL) measurements were conducted at forward bias and the electroluminescence (EL) emission was probed with a silicon detector. The MEL is defined as:

**Simulations.** First-principles calculations based on density functional theory (DFT) are carried out as implemented in the PWSCF Quantum-Espresso package [55]. Geometry optimization, including dispersion correction [56], is performed using PBE functional [57], and the electrons-ions interactions are described by ultrasoft pseudo-potentials [58] with electrons from I 5s, 5p; N, C 2s, 2p; H 1s; Rb 5s; Pb, 6s, 6p, 5d; shells explicitly included in calculations. Geometry optimizations of 2 × 2 × 1 supercell (16 formula units) are performed with a k-point sampling [59] of 1 × 1 × 2 by relaxing both ions and volume along with plane-wave basis set cutoffs for the smooth part of the wave functions and augmented electronic density expansions of 50 and 400Ry, respectively. GGA-SOC band structures have been considered for Rashba splitting and calculated using the method described at Ref. 30.

**Acknowledgments**

M.V. acknowledges support of this work by the project “Development of Materials and Devices for Industrial, Health, Environmental and Cultural Applications” (MIS 5002567) which is implemented under the “Action for the Strategic Development on the Research and Technological Sector”, funded by the Operational Programme “Competitiveness, Entrepreneurship and Innovation” (NSRF 2014-2020) and co-financed by Greece and the European Union (European Regional Development Fund). A.M. and F.D.A. acknowledge European Union’s Horizon 2020 research and innovation programme under Grant Agreement No. 764047 of the ESPRESSO project. The Ministero dell’Istruzione dell’Universitàe della Ricerca (MIUR) and Università degli Studi di Perugia are acknowledged for financial support through the program “Dipartimenti di Eccellenza 2018-2022” (Grant AMIS). W.J.S. and F.K.S. acknowledge the financial support from CNPq, Brazil. ToF-SIMS measurements of this research were conducted at the Center for Nanophase Materials Sciences, which is a DOE Office of Science User Facility.

**References**

[1]

S.D. Stranks, et al.

Science, 342 (2013), pp. 341-344

CrossRef

[2]

T.M. Brenner, et al.

Nat. Rev. Mater., 1 (2016), p. 15007

[3]

D. Shi, et al.

Science, 347 (2015), pp. 519-522

CrossRefView Record in Scopus

[4]

Q.A. Akkerman, et al.

Nat. Energy, 2 (2017), p. 16194

View Record in Scopus

[5]

J.H. Heo, et al.

Nat. Photonics, 7 (2013), pp. 486-491

CrossRef

[6]

S.D. Stranks, H.J. Snaith

Nat. Nanotech., 10 (2015), pp. 391-402

CrossRefView Record in Scopus

[7]

B.P. Sutherland, E.H. Sargent

Nat. Photon., 10 (2016), pp. 295-302

CrossRefView Record in Scopus

[8]

Z.-K. Tan, et al.

Nat. Nanotech., 9 (2014), pp. 687-692

CrossRef

[9]

K. Kang, et al.

Adv. Mater., 31 (2019), p. 1970149

CrossRefView Record in Scopus

[10]

J. Choi, et al.

Adv. Mater., 28 (2016), p. 6562

CrossRefView Record in Scopus

[11]

J. Fing, et al.

Nat. Electron., 1 (2018), pp. 404-410

[12]

Y. Lee, et al.

Adv. Mater., 27 (2015), pp. 41-46

CrossRef

[13]

Q. Lin, et al.

Nat. Photon., 9 (2015), pp. 687-694

CrossRefView Record in Scopus

[14]

L. Shen, et al.

Adv. Mater., 28 (2016), pp. 10794-10800

CrossRefView Record in Scopus

[15]

M.I. Saidaminov, et al.

Nat. Commun., 6 (2015), p. 8724

View Record in Scopus

[16]

Y. Fang, et al.

Nat. Photon., 9 (2015), pp. 679-686

CrossRef

[17]

Q. Han, et al.

Adv. Mater., 28 (2016), pp. 2253-2258

CrossRefView Record in Scopus

[18]

L. Miao, F. Zhang

J. Mater. Chem. C, 7 (2019), pp. 1741-1791

CrossRefView Record in Scopus

[19]

I.M. Asuo, et al.

Nano Energy, 51 (2018), pp. 324-332

ArticleDownload PDFView Record in Scopus

[20]

L. Dou, et al.

Nat. Commun., 5 (2014), p. 5404

View Record in Scopus

[21]

B.R. Sutherland, et al.

ACS Photonics, 2 (8) (2015), pp. 1117-1123

CrossRefView Record in Scopus

[22]

C. Xie, et al.

Light: Sci Appl., 6 (2017), Article e17023

CrossRefView Record in Scopus

[23]

L. Gu, Z. Fan

Light: Sci Appl., 6 (2017), Article e17090

CrossRefView Record in Scopus

[24]

H.-Y. Park, et al.

Adv. Mater., 28 (2016), pp. 864-870

CrossRefView Record in Scopus

[25]

F. Bai, et al.

Adv. Mater. Interfaces, 5 (2018), p. 1701275

CrossRefView Record in Scopus

[26]

C. Ma, et al.

Adv. Mater., 28 (2016), pp. 3683-3689

CrossRefView Record in Scopus

[27]

T. Wang, et al.

Energy Environ. Sci., 10 (2017), pp. 509-515

View Record in Scopus

[28]

F. Zheng, et al.

Nano Lett., 15 (2015), pp. 7794-7800

CrossRefView Record in Scopus

[29]

W. Deng, et al.

Nano Lett., 17 (2017), pp. 2482-2489

CrossRefView Record in Scopus

[30]

T. Etienne, E. Mosconi, F. De Angelis

J. Phys. Chem. Lett., 7 (2016), pp. 1638-1645

CrossRefView Record in Scopus

[31]

Y. Zhai, et al.

Sci. Adv., 3 (2017), Article e1700704

View Record in Scopus

[32]

J. Yin, et al.

Chem. Mater., 30 (23) (2018), pp. 8538-8545

CrossRefView Record in Scopus

[33]

S.B. Todd, et al.

APL Materials, 7 (2019), Article 081116

CrossRefView Record in Scopus

[34]

Z. Chen, et al.

Nat. Commun., 8 (2017), p. 1890

View Record in Scopus

[35]

K. Frohna, et al.

Nat. Commun., 9 (2018), p. 1829

View Record in Scopus

[36]

Y. Chen, et al.

Nature, 577 (2020), pp. 209-215

[37]

B. Wu, et al.

Nat. Commun., 10 (2019), p. 484

CrossRef

[38]

D. Niesnera, et al.

Proc. Natl. Acad. Sci., 115 (2018), pp. 9509-9514

[39]

N.J. Jeon, et al.

Nature, 517 (2015), pp. 476-480

CrossRefView Record in Scopus

[40]

A. Amat, et al.

Nano Lett., 14 (6) (2014), pp. 3608-3616

CrossRefView Record in Scopus

[41]

M. Saliba, et al.

Science, 354 (2016), p. 206

CrossRef

[42]

G. Dresselhaus, A.F. Kip, C. Kittel

Phys. Rev., 95 (1954), pp. 568-569

View Record in Scopus

[43]

E.I. Rashba

Phys. Solid State, 2 (1960), pp. 1224-1238

[44]

B. Cao, et al.

J. Mater. Chem. A, 7 (2019), pp. 4960-4970

CrossRefView Record in Scopus

[45]

Y. Yue, et al.

ACS Energy Lett., 2 (5) (2017), pp. 1177-1182

[46]

D.W. De Quilettes, et al.

Science, 348 (2015), pp. 683-686

CrossRefView Record in Scopus

[47]

T. Hwang, et al.

ACS Appl. Mater. Interfaces, 11 (7) (2019), pp. 6907-6917

CrossRefView Record in Scopus

[48]

D. Azulay, et al.

Phys. Chem. Chem. Phys., 20 (2018), pp. 24444-24452

CrossRefView Record in Scopus

[49]

H. Jin, et al.

Mater. Horizon, 7 (2020), pp. 397-410

CrossRefView Record in Scopus

[50]

V. Capozzi

Phys. Rev. B, 23 (1981), pp. 836-840

View Record in Scopus

[51]

W.J. Zhao, et al.

Nano Lett., 13 (2013), pp. 5627-5634

CrossRefView Record in Scopus

[52]

A. Manchon, et al.

Nat. Mater., 14 (2015), pp. 871-882

CrossRefView Record in Scopus

[53]

J. Wang, et al.

Nat. Commun., 10 (2019), p. 129

ArticleDownload PDF

[54]

C. Zhang, et al.

Nat. Phys., 11 (2015), pp. 427-434

CrossRefView Record in Scopus

[55]

P. Giannozzi, et al.

J. Phys.: Condens. Matter., 21 (2009), Article 395502

CrossRefView Record in Scopus

[56]

S. Grimme, J. Antony, S. Ehrlich

J. Chem. Phys., 132 (2010), Article 154104

CrossRefView Record in Scopus

[57]

J.P. Perdew, K. Burke, M. Ernzerhof

Phys. Rev. Lett., 77 (1996), pp. 3865-3868

[58]

D. Vanderbilt

Phys. Rev. B, 41 (1990), p. 7892

[59]

H.J. Monkhorst, J.D. Pack

Phys. Rev. B, 13 (1976), pp. 5188-5192

[60]

J. Wang, et al.

Adv. Mater., 28 (2016), pp. 8302-8308